Evaluation of task-specific ionic liquids applied in pervaporation membranes: experimental and COSMO-RS studies

Xiao Xu [a,b], Gilles Van Eygen [a, b, c], Cristhian Molina-Fernández [a, b], Daria Nikolaeva [a,b], Ysaline Depasse [a, b], Sara Chergaoui [a,b,] Yusak Hartanto [a,b], Bart Van der Bruggen [c], João A.P. Coutinho [d], Anita Buekenhoudt [e], Patricia Luis [a,b]

[a] *Institute of Mechanics, Materials and Civil Engineering - Materials & Process Engineering (iMMC-IMAP), UCLouvain, Place Sainte Barbe 2, 1348 Louvain-la-Neuve, Belgium*

[b] *Research & Innovation Centre for Process Engineering (ReCIPE), Place Sainte Barbe, 2 bte L5.02.02 - B-1348 Louvain-la-Neuve (Belgium)*

[c] *Process Engineering for Sustainable Systems (ProcESS), Katholieke Universiteit Leuven, Celestijnenlaan 200f, 3001 Leuven, Belgium*

[d] *CICECO-Aveiro Institute of Materials, Chemistry Department, University of Aveiro, 3810-193 Aveiro, Portugal*

[e] *Unit Separation and Conversion Technology, Vlaamse Instelling voor Technologisch Onderzoek (VITO NV), Boeretang 200, 2400 Mol, Belgium*

Corresponding authors: xiao.xu@uclouvain.be

patricia.luis@uclouvain.be

Abstract

The production of dimethyl carbonate (DMC) from CO_2 and methanol (MeOH) is an attractive route for CO_2 capture and utilization. In this process, the separation of DMC from the reaction medium is critical to maximize the conversion of CO_2. However, DMC and MeOH form an azeotropic mixture that is difficult to separate. This work investigates the possibility of using task-specific ionic liquids (TSILs) in the form of supported ionic liquid membranes (SILMs) to separate and purify DMC by using pervaporation. Two tertiary amine ILs, i.e., 1-octyl-3-methylimidazolium bromide ([Omim][Br]) and 1-octyl-3-methylimidazolium bis(trifluoromethanesulfonyl)imide ([Omim][NTf2]), and one cyclic quaternary ionic liquid, i.e., 1-octyl-1,4-diazabicyclo[2.2.2]octanium bromide ([ODABCO][Br]), were prepared. The structure and purity of the synthesized ILs were confirmed by NMR and FTIR, and the as-synthesized ILs along with one commercial quaternary ammonium IL, tetrabutylammonium bromide ([TBA][Br]), were further characterized using TGA/DSC. SEM-EDX, tensile tests and stability tests were also performed to characterize the SILMs. During the pervaporation experiments, the SILMs showed an initial decrease in DMC and MeOH permeance over time, followed by a gradual stabilization, with a relatively stable DMC/MeOH selectivity as pure liquids. In addition, an increase in temperature is shown to have negative effect on DMC and MeOH permeance because sorption, which is an exothermic process, governed the transport of molecules across the membrane. The studied SILMs exhibited higher selectivity at low temperatures, especially at 30 ℃. Furthermore, the COSMO-RS model provided insights of the effect of IL structures on the separation of DMC from MeOH at molecular level.

Keywords: Dimethyl carbonate, methanol, ionic liquids, supported ionic liquid membranes, pervaporation, COSMO-RS model

1. Introduction

Dimethyl carbonate (DMC) is a carbonate ester that occurs in liquid form at room temperature. It is transparent, colourless, non-corrosive and biodegradable[1]. DMC can be used as a reagent for biodiesel production [2], an intermediate chemical for the synthesis of polycarbonates [3, 4], an electrolyte in lithium batteries [5, 6], and an efficient and alternative fuel additive [7, 8]. Therefore, the annual demand for this chemical has increased rapidly during the past decade due to DMC's various green and sustainable applications [9].

Until now, several production routes have been applied to synthesize DMC, including carbon dioxide (CO_2)–methanol (MeOH) synthesis, oxidative carbonylation, and urea methanolysis [10, 11]. Among these, the route of direct synthesis of DMC from CO_2 and MeOH has attracted attention because it can contribute to the reduction of CO_2 emissions. As MeOH can be also produced by the hydrogenation of CO_2, three moles of CO_2 could be totally consumed to produce one mole of DMC, which is beneficial for CO_2 fixation[12]. However, DMC synthesis from MeOH and CO_2 is a tough task because of thermodynamic equilibrium limitations[13] and kinetic inertness[14]. Its chemical transformation therefore usually requires harsh reaction conditions, and often requires complex and expensive catalytic systems, such as 2-cyanopyridine and CeO_2 catalytic combination[15, 16]. Ionic liquids (ILs) are organic salts with a low melting point. They are composed of an organic cation and an inorganic or organic anion [17, 18] and exhibit many attractive properties such as good chemical and thermal stabilities as well as their negligible vapour pressure [17, 19]. In addition, the chemical and physical properties of ILs can be modified by combining different cations and anions or tailoring the length and branching of the alkyl chains, thereby obtaining "design solvents" used widely in catalysis[20]. ILs have also demonstrated to be effective catalysts for the transformation of CO_2 and MeOH to DMC, especially $[N_{114,6N11}]X$ (X = Cl, Br, I) with a tertiary amino moiety and a quaternary ammonium group showing significant catalytic efficiencies [12, 21].

After reaction, the separation of DMC from MeOH also presents challenges. DMC forms an azeotrope mixture with MeOH under different concentrations at different pressures[22, 23], the separation step of this mixture involves significant energy consumption[24]. Pervaporation is a promising alternative technology to conventional distillation when the energy penalty becomes high due to the presence of azeotropes or close-boiling point components [25, 26]. Nonetheless, the development of high-performance membranes for the pervaporative recovery of DMC from MeOH/DMC mixtures is still an important obstacle to be addressed. As mentioned above, the tunability of ILs can be used to provide high selectivity to target molecules in the separation [27, 28], which encourages to evaluate the performance of supported ionic liquid membranes (SILMs), with the additional advantage of using a small amount of ILs to fill the membrane pores so that there is no need to recycle them.

Inspired by the different roles of ILs, hereat, two tertiary amine ILs, i.e., 1-octyl-3-methylimidazolium bromide ([Omim][Br]) and 1-octyl-3-methylimidazolium bis(trifluoromethanesulfonyl)imide ([Omim][NTf2]), and one cyclic quaternary IL, i.e., 1-octyl-1,4-diazabicyclo[2.2.2]octanium bromide ([ODABCO][Br]) were synthesized, and then the as-synthesized ILs as well as one commercial quaternary ammonium IL, i.e., tetrabutylammonium bromide ([TBA][Br]) were used to prepare SILMs. By combining task-specific ILs with membrane technologies, the advantages of membrane separation processes (easy operation, small unit size, low environmental impact, high energy efficiency, etc) are integrated with the tuneable properties of ILs to endow these new materials with unprecedented characteristics [29]. Moreover, the combination of ILs and membrane separation processes can lead to new efficient way to separate valuable products from complex mixtures, like esterification reaction mixture, and reducing multiple steps for the reaction-separation processes at the same times.

SILMs have found wide applicability in gas separation (e.g., the separation of SO_2/CO_2, $CO_2/H_2/N_2$, $H_2S/CO_2/CH_4$ and natural gas purification) [29-41]. However, SILMs have not so far been utilized much used in liquid separation, specifically in pervaporation, due to the difficulties associated to the selection of a suitable pervaporative SILM for a target compound with good permeance, and the lack of stability of supported liquid membranes. In the present study, two tertiary amine ILs and two quaternary ammonium ILs have been used for the fabrication of SILMs that can retain all the advantages of a membrane system and further provide the catalytic potential for the direct synthesis of DMC using CO_2 and MeOH. The permeance of DMC and MeOH through SILMs was then measured in a pervaporation set-up allowing the ideal selectivity to DMC/MeOH mixture to be computed based on permeances of the pure solvents. Furthermore, the stability of SILMs was investigated. The pervaporative performance of four ILs was also simulated *in situ* by the quantum-chemical model COSMO-RS for affording some theoretical insights into the separation of DMC from MeOH at the molecular scale using SILMs.

2. Materials and methods

2.1 Chemicals

Acetonitrile (≥ 99.8%), acetic acid (≥ 99.0%), bis(trifluoromethane)sulfonimide lithium salt (≥ 99.0%), 1-bromooctane (≥ 99.0%), dimethyl carbonate (≥ 99.0%), 6-chlorohexanol (≥96.0%), cyclohexane (≥ 99.5%), 1,4-diazabicyclo[2.2.2]octane (Dabco), (≥ 99.0%)), diethyl ether (≥ 99.0%), ethanol (≥99.0%), sodium hydroxide (≥97.0%), 1,3-diaza-2,4-cyclopentadiene (imidazole, ≥99.0%), methanol (≥99.8%), 1-methylimidazole (≥99.0%), 4-methylmorpholinStrontium hydroxide octahydratee (≥99.0%), potassium sulphate (≥99.0%), sodium hydrogen sulphate (≥95.0%) and tetrabutylammonium bromide (≥98.0%) were all purchased from Sigma Aldrich (USA). The ultrafiltration membrane used as a support made of polyacrylonitrile (PAN) was manufactured by Synder Filtration (USA). Tetrabutylammonium bromide ([TBA][Br]) (≥98.0%) was provided by Sigma Aldrich (USA).

2.2 IL preparation and spcetroscopy characterization

The ILs [Omim][Br] and [ODABCO][Br] were prepared by quaternization reaction in acetonitrile[42, 43]. Once prepared, these ILs were purified by washing with cyclohexane and diethyl ether. [Omim][NTf2] was obtained from [Omim][Br] by metathesis reaction[44]. Fig. 1 provides information about the experimental conditions of these reactions. The chemical structures and purity of ILs was confirmed by NMR and FTIR spectroscopy (Perkin Elmer Spectrum 100 FTIR with Universal ATR Sampling Accessory).

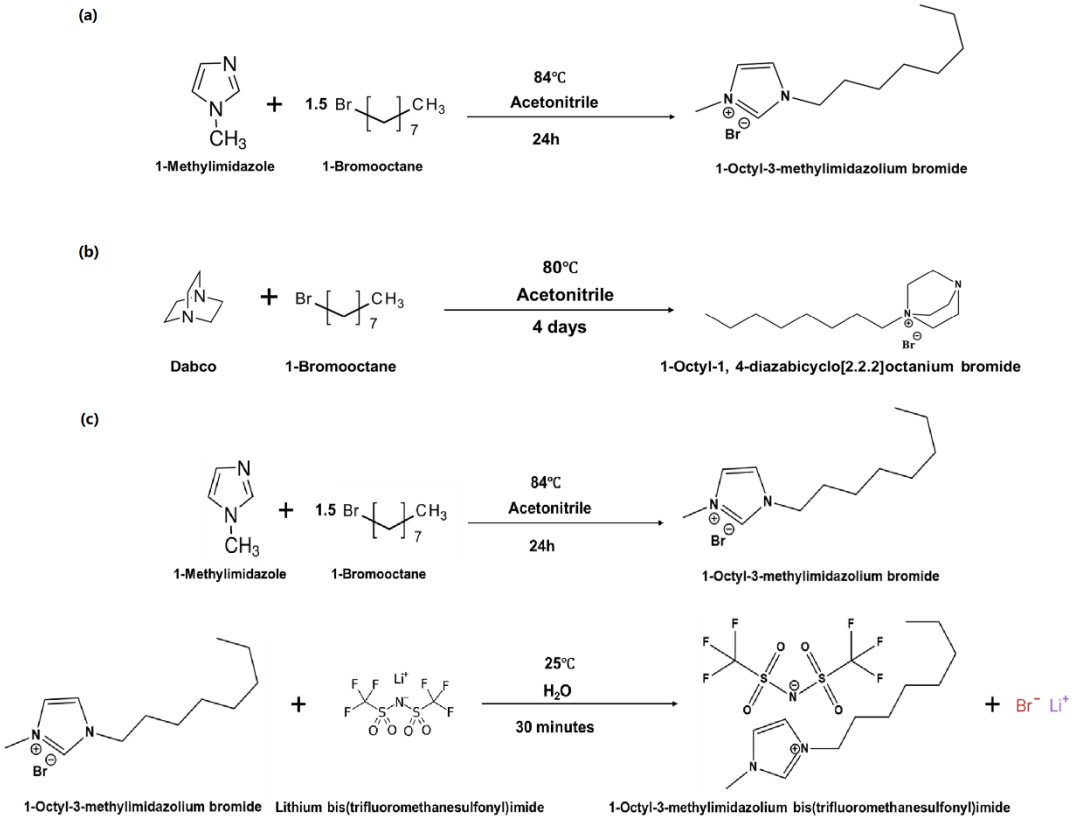

Fig. 1. Synthetic route of (a) [Omim][Br], (b) [ODABCO][Br] and (c) [Omim][NTf2].

2.3 Thermal analysis of ILs

The thermal stability of the ILs was investigated by Thermo Gravimetric Analysis (TGA) using a TGA/SDTA 851e (Mettler-Toledo, Switzerland), as illustrated in **Fig. S12**. Samples of 10 mg were heated from room temperature to 600 °C with a constant heating rate of 10 °C/min. Differential Scanning Calorimetry (DSC) was carried out on a Pyris Diamond apparatus from Perkin Elmer. Samples of 10 mg placed into aluminium pans were scanned at a heating rate of 10 °C/min under continuously purging nitrogen gas atmosphere.

2.4 SILM preparation

SILM membranes containing [1O3MIm[Br] and [Omim][NTf2] were prepared using the membrane cell of the pervaporation set-up. The detailed procedure to prepare the SILMs can be found elsewhere [28]. In summary, a circular piece of flat sheet PAN membrane (supporting membrane) was placed into the membrane cell. Vacuum was applied to keep the membrane surface flat. Subsequently, the rubber O-ring was tightly mounted on the circular membrane. Then, a suitable amount of IL was then poured to cover evenly the top surface of the membrane, as illustrated in Fig. 2. Next, the membrane cell was fixed and tightened by closing the clamps. A vacuum of < 1mbar was applied on the permeate side for 2 hours to suck the IL into the membrane pores. After the impregnation of IL, excess IL on the membrane surface was carefully removed with paper tissues. For the Ils [ODABCO][Br] and [TBA][Br], as they are solid at room temperature, 40 wt.% IL solutions were prepared using deionised water.

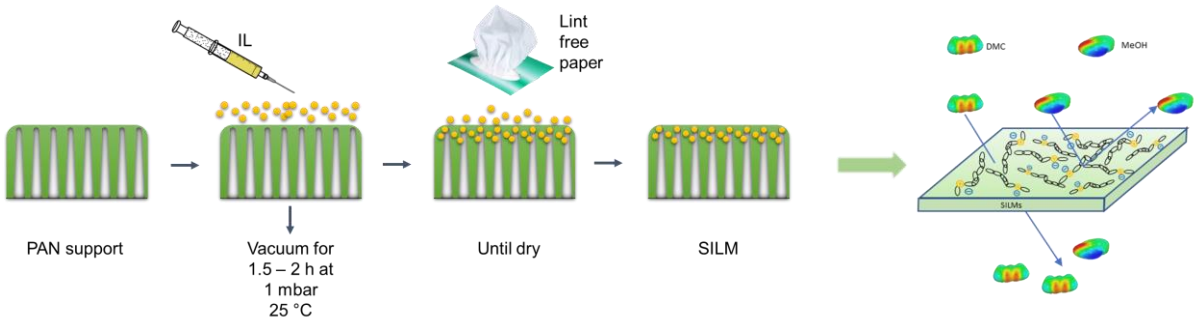

Fig. 2. Schematic illustration of the preparation of SILMs

2.5 SEM-EDS characterization of SILMs

To evaluate the quality of the impregnation of Ils inside the porous support, the morphology of the cross section of PAN and SILMs was analysed by SEM (Zeiss, ULTRA with Bruker EDS chemical analyser). Beforehand, the membranes were immersed in liquid nitrogen and were cut into small rectangular samples. The membrane samples were coated with a thin layer of gold (Quorum Q150 RS) to make them conductive. An analysis with energy dispersive spectrometer (EDS) was also used to investigate the overall chemical composition and the distribution of the chemical elements of interest in the membranes.

2.6 SILM mechanical properties

A tensile test was carried out on the various SILMs produced in order to analyse the elastic behaviour of the various membranes as well as their degree of resistance to breakage. Tensile tests were conducted using a tensile test instrument (Model Zwick Roel, Germany). The test samples were cut with dimensions of 5 ×7 cm. Each sample was then placed between two jaws, 45.29 mm apart from each

other with a crosshead speed of 2 mm / min. The testXpert® software was used to acquire the characteristic curves. For each membrane, three samples were tested.

2.7 SILM static stability

In order to evaluate SILM stability towards MeOH and DMC, a piece of each freshly prepared SILM was immersed in pure MEOH or DMC during 1 and 7 days at room temperature. The weight was measure before and after the immersion period and the stability was evaluated by the relative mass loss (equation 1). Pristine PAN was also immersed for comparison.

$$\text{Relative mass loss (\%)} = (\text{initial mass} - \text{final mass})/\text{initial mass}*100 \quad (1)$$

2.8 Pervaporation experiments

The pervaporation experiments were performed using a pervaporation setup (Sulzer Chemtech GmbH, Switzerland) (Fig. 3). It is the same unit used to prepare the SILMs.

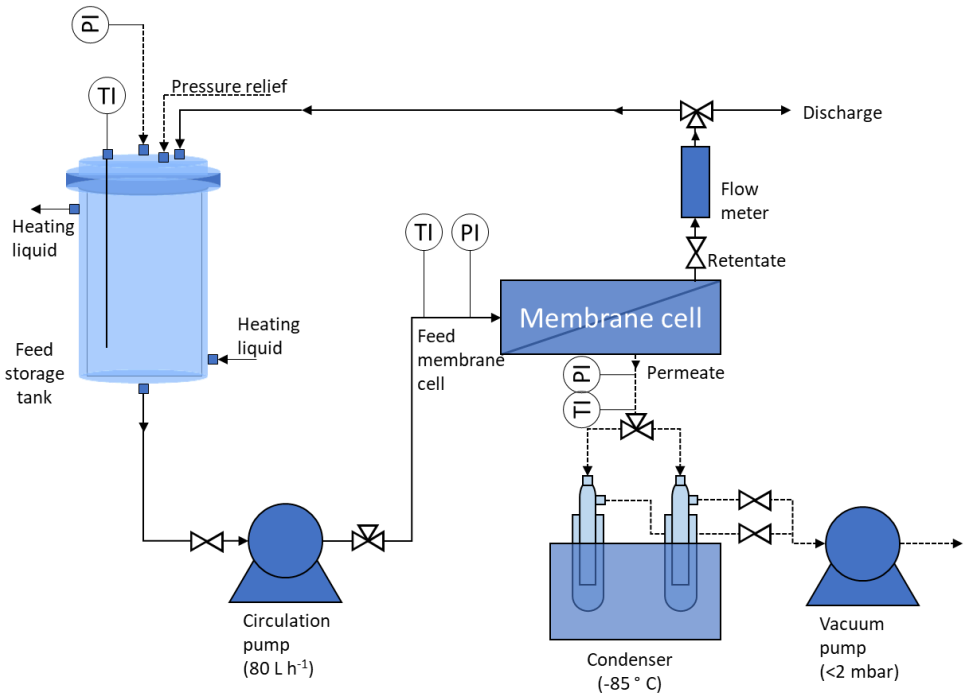

Fig. 3. The scheme of pervaporation separation experimental equipment.

In the pervaporation experiments, the permeate side was evacuated using a vacuum pump to give a vacuum pressure of 1–3 mbar. The surface area of installed SILMs was 38.48 cm^2 (diameter 7.0 cm). The permeate was collected and weighed in certain intervals relying on the amount of the permeate. The prepared SILMs were tested at different temperatures (30±0.5°C, 40±0.5°C and 50±0.5°C) using two different pure feed solvents (MeOH and DMC).

The performance of SILMs was evaluated by permeance $\bar{P}$ (GPU, with 1 GPU = 1×10^{-6} cm^3(STP)/cm^2 s cm Hg, and 1 m^3 m/m^2 s kPa = 1.33×10^8 GPU) and selectivity α_{ij}, expressed as follows[45]:

$$J = \frac{Q}{t \times A} \quad (2)$$

$$\bar{P} = \frac{J_i}{x_i \cdot \gamma_i \cdot p_i^{sat} - y_i p^p} \quad (3)$$

$$\alpha_{ij} = \frac{\bar{P}_i}{\bar{P}_j} \quad (4)$$

in which A is the membrane effective area (m^2), t is the permeate collecting time (h), Q is the weight of permeate (kg), γ_i is the activity coefficient and p_i^{sat} is the saturated vapor pressure of component i; x_i and y_i are the mole fractions of component i in feed and permeate, respectively, and p^p is the total pressure at the permeate side.

Membrane selectivity is defined as the ratio of the permeances of components i and j through the membrane. Selectivity also helps to determine the ability of the membrane to force the diffusion of a specific species.

2.9. COSMO-RS simulations

The TmoleX v.4.5 software package was used to perform the quantum calculations using the density functional theory (DFT) with a resolution identity (RI) approximation. The optimized geometries of the considered cations and anions were obtained using a triple zeta valence polarised basis set (def-TZVP), the Becke-Perdew (BP-86) functional level of theory and the COSMO solvation model and were stored as COSMO-files. Next, vibrational frequency calculations were executed to confirm the presence of an optimized energy state. Finally, the generated COSMO-files were used as input in COSMOthermX to predict the thermodynamic properties of the ILs [46-48].

3. Results and discussion

3.1. NMR and FTIR of the synthesized ILs

The ILs were successfully synthesized, which showed consistency with literatures [49-51]. The products were confirmed by FTIR, ^{1}H NMR, and ^{13}C NMR spectroscopy. The results of the synthesized ILs are below.

NMR:

1-octyl-3-methylimidazolium bromide ([Omim][Br]). ^{1}H NMR (500 MHz, $CDCl_3$) δ: 10.23 (s, 1H), 7.61 (t, J = 1.8 Hz, 1H), 7.42 (t, J = 1.8 Hz, 1H), 4.24 (dd, J = 7.5 and 7.3 Hz, 2H), 4.05 (s, 3H), 1.83 (quint, J = 7.5 Hz, 2H),1.30-1.10 (m, 10H), 0.78 (t, J = 7.0 Hz, 3H). ^{13}C{^{1}H}F NMR (125 MHz, $CDCl_3$) δ: 137.2, 128.8, 122.0, 50.0, 36.7, 31.6, 30.3, 28.9, 28.8, 26.2, 22.5, 14.0.

1-Octyl-1,4-diazabicyclo[2.2.2]octanium bromide ([ODABCO][Br]). ^{1}H NMR (500 MHz, CDCl3) δ: 3.61 (t, J = 7.5 Hz, 6H), 3.41-3.38 (m, 2H), 3.19 (t, J= 7.5 Hz, 6H), 1.72-1.66 (m, 2H), 1.32-1.10 (m, 10H), 0.79 (t, J = 7.0 Hz, 3H). ^{13}C{^{1}H NMR (125 MHz, $CDCl_3$) δ: 64.6, 52.4, 45.4, 31.5, 29.1, 29.0, 26.3, 22.5, 22.1, 14.0.

1-Octyl-3-methylimidazolium bis(trifluoromethanesulfonyl)imide ([Omim][NTf2]). ^{1}H NMR (500 MHz, CD_3OD) δ: 8.74 (s, 1H), 7.32 (t, J = 1.8 Hz, 1H), 7.29 (t, J = 1.8 Hz, 1H), 4.15 (dd, J = 7.6 and 7.4 Hz, 2H), 3.93 (s, 3H), 1.85 (quint, J = 7.5 Hz, 2H), 1.30-1.18 (m, 10H), 0.86 (t, J = 7.0 Hz, 3H). ^{13}C{^{1}H} NMR (125 MHz, CD_3OD) δ: 136.1, 123.8, 122.3, 119.9 (1J13C-19F = 320.5 Hz, 2C), 50.3, 36.4, 31.7, 30.2, 29.0, 28.9, 26.2, 22.6, 14.1.

FTIR:

[Omim][Br]: 3420: symmetric stretching of OH; 3139, 3066: C–H stretching of imidazole ring; 2960, 2927, 2859: aliphatic stretching of C–H; 1737: absorbed water; 1630: O–H bending; 1570: Imidazole ring stretching; 1464: asymmetric deformation vibrations of CH_3 and CH_2; 1377: symmetric deformation vibration of CH_3; 1166: Imidazole ring H–C–C & H–C–N bending; 844: N–C(H) –N–CH bending, C–CH bending and octyl bending; 752: Out-of-plane C–H bending of imidazole ring.

[ODABCO][Br]: 3330: symmetric stretching of OH; 3147, 3068: C–H stretching of $[ODABCO]^+$ ring; 2931, 2861: aliphatic stretching of C–H; 1738: adsorbed water, 1634: O–H bending; 1570: $[ODABCO]^+$ ring stretching; 1458: asymmetric deformation vibrations of CH_3 and CH_2; 1371: symmetric deformation vibration of CH_3; 1168: ring H–C–C & H–C–N bending; 1056: C–C & C–N stretching; 856: N–C(H) –N–CH bending, C–CH bending and octyl bending; 760: C–N stretching; 732: CH_2 twisting.

[Omim][NTf2]: 3154, 3118: C–H stretching of imidazole ring; 2931, 2859: aliphatic stretching of C–H; 1571: Imidazole ring stretching; 1463: asymmetric deformation vibrations of CH_3 and CH_2; 1349: SO_2 asymmetric deformation vibrations of $[NTf2]^{-1}$, and $(N)CH_2$ stretching; 1329: C–N/C=N stretching of imidazole ring; 1225: SO_2 asymmetric stretching of the anion; 1181: H–C–C & H–C–N bending of imidazole ring; 1133: symmetric stretching of CF_3; 1054: S–N–S asymmetric stretching; 843: in-plane C–H bending peak of imidazolium ring; 789: C–S & S–N stretching; 763: S–N–S symmetric stretching; 740: CF_3 symmetric bending.

All the above results confirm the purity and structure of the synthesized ILs shown in (Fig. S1-S7).

3.2. Thermal analysis of ILs

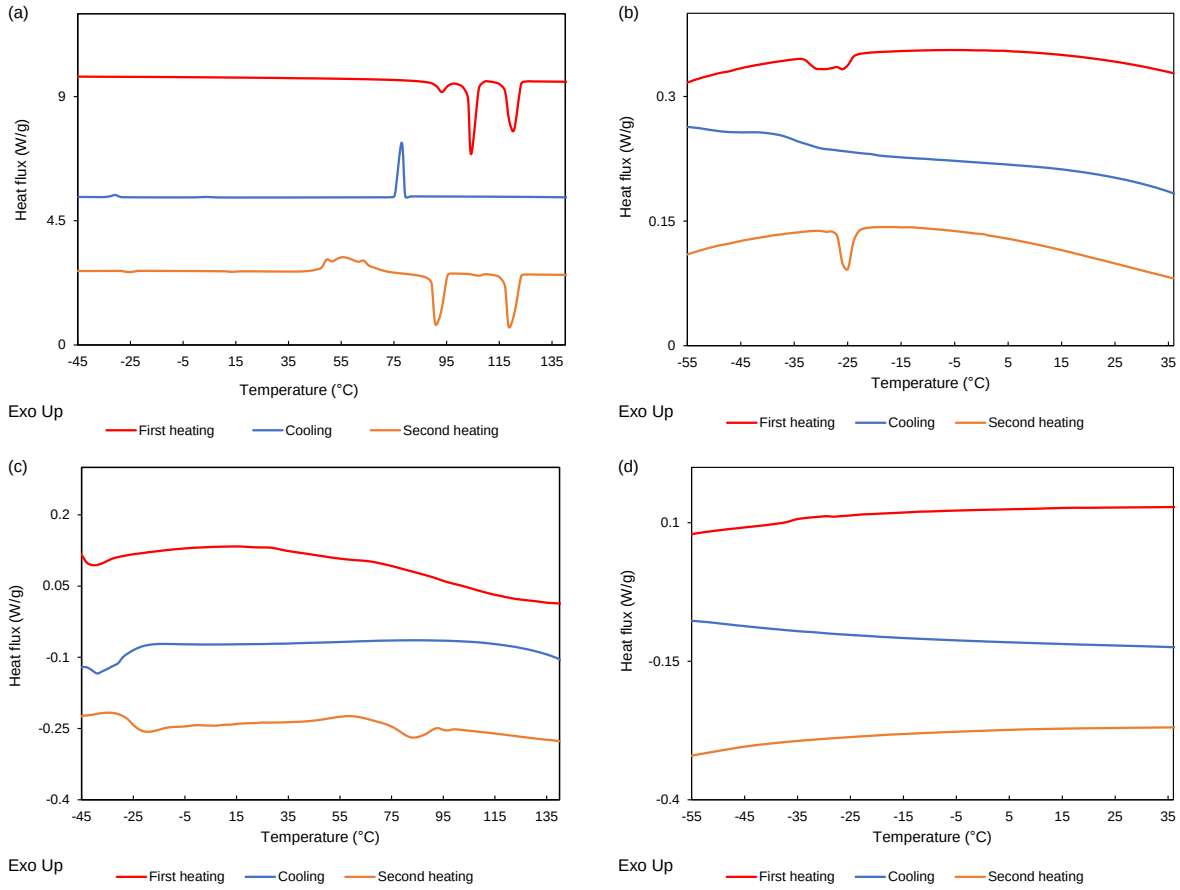

Fig. 4. DSC thermograms of (a) [TBA][Br], (b) [Omim][Br], (c) [ODABCO][Br], and (d)[Omim][NTf2].

The thermal properties of 4 different ILs were studied by using TGA (Fig. S8) and DSC. In order to investigate further the melting and crystallization behavior of ILs, DSC was carried out. The DSC curves of ILs are shown in Fig. 4. For [TBA][Br], two additional solid-solid phase transitions besides the melting transition are detected on the first heating run, while a transition is detected in the cooling run corresponding to crystallization to a second crystalline phase (Cr'). This crystalline state (Cr') is not thermodynamically stable at higher temperature and goes to the first crystalline phase (Cr) at temperature above around 49 ℃ during the second run. The first heating run for [Omim][Br] shows only one transitions corresponding to the melting process, while no transitions were detected in the cooling run. Hence, the re-crystallization fails and a glassy solid is formed. The thermal characteristic for the second run almost remains constant, suggesting that [Omim][Br] forms a glassy state rather than crystallizing. Only a very small effect, a glass transition around -45 ℃, for [ODABCO][Br] can be detected on the first heating run, without any obvious sharp peak. Three events are observed on the second heating, a glass transition around -45 ℃ and a broad exothermic peak starting from about 40 ℃ (crystallization of amorphous material), followed by a broad melting peak. The measurements of [Omim][NTf2] lead to straight line thermograms without obvious signal, very different from

[Omim][Br] containing the same cation. This can be attributed to the bulkiness, low structural symmetry, molecular flexibility, and charge delocalization of the [NTf2] anion[52].

3.3. Membrane characterisation

3.3.1. SEM and EDS

After immobilization of the ILs [TBA][Br], [Omim][Br], [ODABCO][Br] and [Omim][NTf2] in the PAN membrane using vacuum, the PAN membrane and SILMs were characterized to confirm the complete immobilization of the ILs on the support membrane surfaces using SEM. The cross section of PAN membrane is shown in Fig. 5a. The cross section of SILMs displayed a very thin IL layer (Fig. 5b-e). EDS analysis further proved that IL layers were successfully immobilized on PAN membranes by detecting the Br and F signals of the ILs at membrane surface.

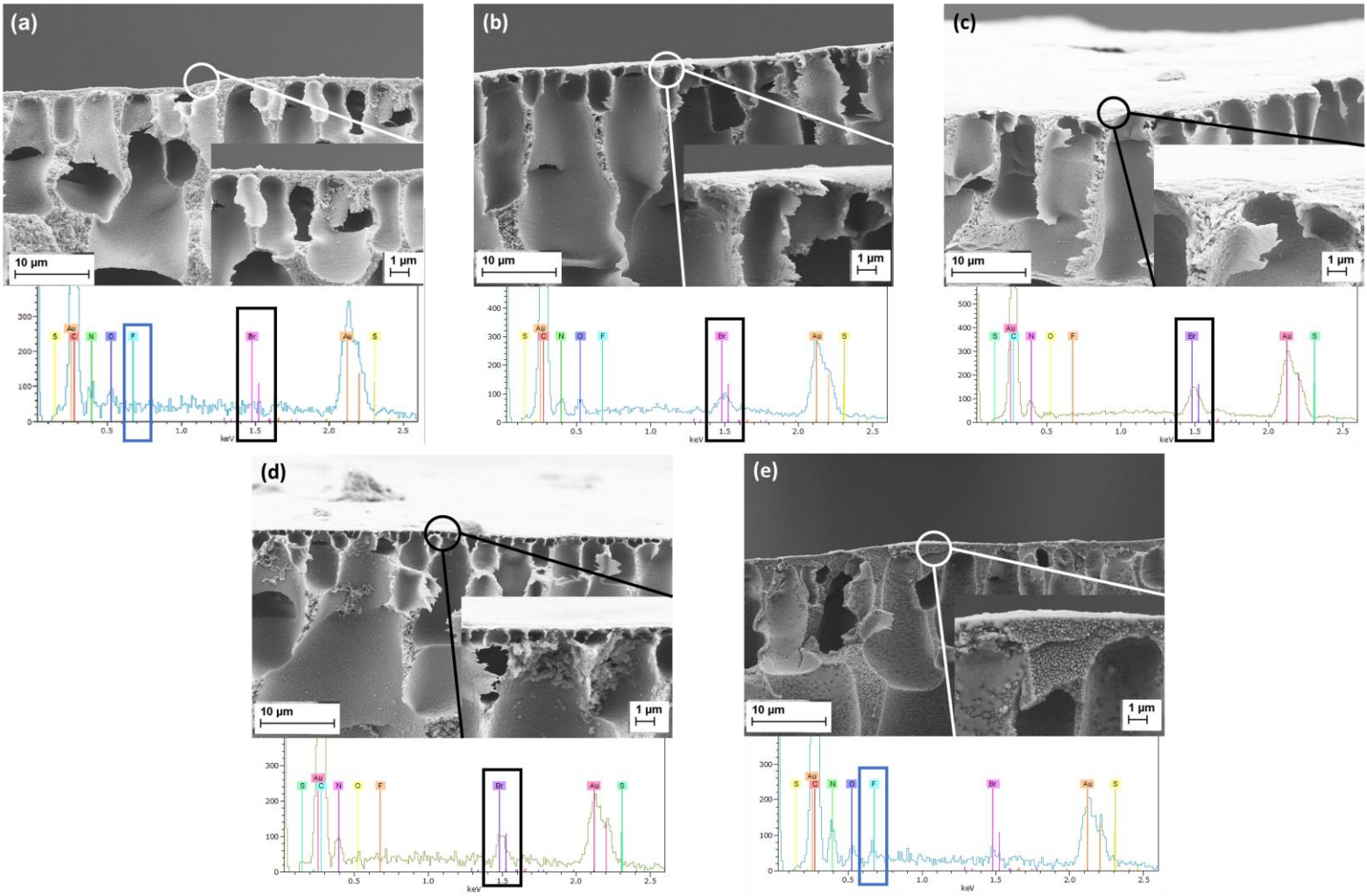

Fig. 5. SEM and EDS results of (a) PAN membrane, (b) SILMs based on [TBA][Br], (c) [Omim][Br], (d) [ODABCO][Br] and (e) [Omim][NTf2].

3.3.2. Tensile tests

Fig. 6. shows the typical tensile-strain behaviours obtained with PAN and SILMs, and the corresponding tensile data are summarized in Table 1. Here, the impregnation of ILs within PAN membranes induced a decrease of the ductility compared to the neat PAN membrane (Fig. 6a and Fig. 6b). The ILs penetrated into the support pores and between the polymer particles and fibres reorienting their structures to an energy-favourable position, destroying the inherent structure of the support membrane, resulting in a decrease in the mechanical stability of the membrane [53]. In addition, this mechanical property largely depends on the quality of the membrane because every small defect can result in precocious fracture[54]. Furthermore, it can be observed that the impregnation of ILs also led to a decrease in the elastic modulus (Fig. 6b). Interestingly, [Omim][NTf2] and [Omim][Br], both having the same cation, induce similar mechanical properties, suggesting that the cation has dominant role on the mechanical properties.

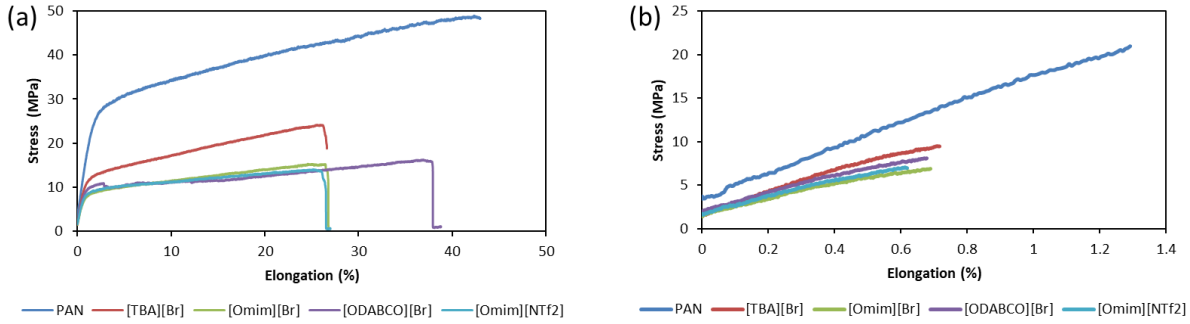

Fig. 6. Stress strain curves of PAN and SILMs (a) and reversible elastic deformation domains of PAN and SILMs (b).

Table 1. Typical parameters in stress-strain curves of PAN and SILMs

Membrane	Tensile strength (MPa)	Elongation at break (%)	Yield strength (MPa)	Young's Modulus (GPa)
PAN	48.6	43.0	20.7	13.83
SILM with [TBA][Br]	24.1	26.1	9.5	11.68
SILM with [Omim][Br]	15.2	26.7	6.9	8.02

SILM with [ODABCO][Br]	16.1	37.8	8.1	9.39
SILM with [Omim][NTf2]	14.0	26.0	7.0	8.91

307

308 3.3.3 Supported liquid membrane stability tests

309 The stability of immobilized ionic liquids was determined by examining the static weight loss of the
310 SILMs in DMC and MeOH, respectively, for a certain period of time (Fig. 7). Except for the SILM of
311 [ODABCO][Br], the loss of mass measured after 24 hours, and 168 hours is almost identical. For
312 [TBA][Br] and [Omim][Br], MeOH exhibited the same tendency to dissolve these two ILs while DMC
313 dissolved more [TBA][Br] than [Omim][Br]. Similar to the static case, SILM of [Omim][Br] exhibited
314 higher weight loss of IL after 8-hour MeOH pervaporation at 30 ℃, while SILM of [Omim][Br]
315 exhibited higher dynamic stability for 8-hour DMC pervaporation at 30 ℃, as shown in Fig. S9. In the
316 dynamic situation, the loss of IL is not only from its dissolution in the solvent, but also from leaching
317 through cracks or holes in the support membrane. The support membrane plays a nonnegligible role in
318 the pervaporation application of SILMs, and a high-integrity support membrane can enable good
319 retention of ILs during pervaporation, as observed from Fig. S10.

320 It may be concluded that the stability of SILMs is mainly regulated by the IL's affinity to each solvent
321 [55]. In the case of [ODABCO][Br], a large difference is observed in DMC between the measurement
322 carried after 24 hours and after 168 hours. The reason is that this IL can react with the DMC, and thus
323 the longer these two components contact, the longer the reaction continues, reducing the amount of
324 ionic liquid in the pores of the support [56]. It was found that the stability of SILMs was also dependent
325 on the anion composition of ILs in addition to the dependence of the cation. For example, SILM of
326 [Omim][NTf2] exhibited greater mass loss compared to SILM of [Omim][Br] because of lower
327 viscosity caused by the bulkiness, low structural symmetry, molecular flexibility, and charge
328 delocalization of the [NTf2] anion (as mentioned in Section 3.2). In general, with the exception of
329 [ODABCO][Br], the ILs within the pores of PAN cannot easily be removed in contact with DMC and
330 MeOH indicating that the SILMs are stable.

331

332

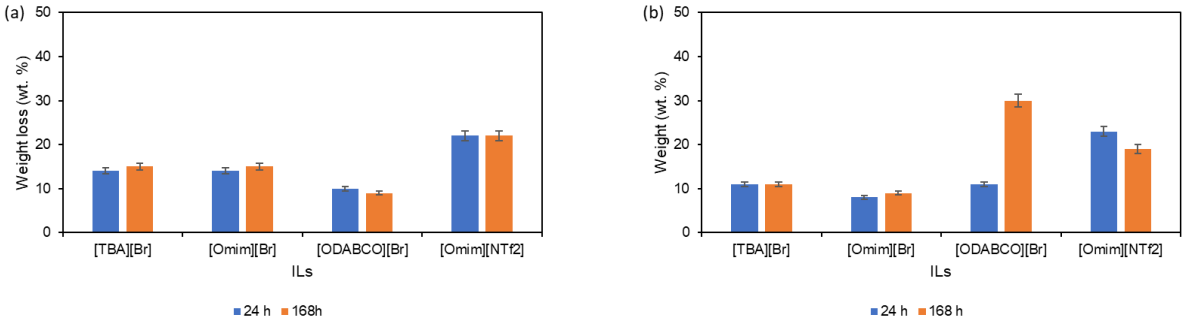

Fig. 7. Weight loss (wt. %) of SILMs measured after immersion in MeOH (a) and DMC (b) for a certain period of time.

3.4 Pervaporation performance of SILMs

3.4.1. Evaluation of liquid permeance and selectivity of SILMs along time

Fig. 8 shows the permeance of DMC for four different SILMs over time. The DMC permeance trends are rather similar for all the membranes, decreasing fast during the initial 90-120 min until reaching a steady state. The SILM with [TBA][Br] showed the lowest permeance.

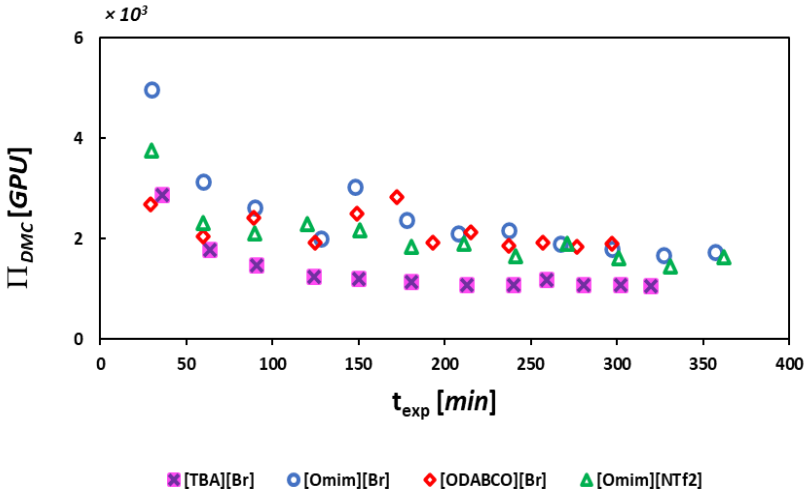

Fig. 8. DMC permeance in PAN membrane and SILMs with four different ILs, T= 40 °C.

A similar pattern of permeance rate was also observed for MeOH, as shown in Fig. 9. The MeOH permeance of all the membranes was lower than the DMC permeance, because the DMC separation is mainly driven by solubility differences between DMC and MeOH in the membranes (see section 3.3). The permeance of MeOH for SILMs with [TBA][Br], [ODABCO][Br] and [Omim][NTf2] exhibited almost equivalent values while it was significantly higher for the SILM with [Omim][Br].

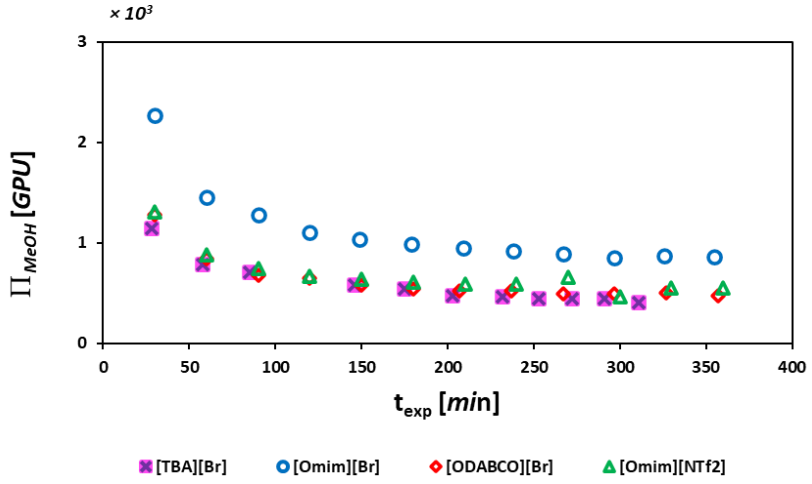

Fig. 9. MeOH permeance in PAN membrane and SILMs of four different ILs, T= 40 ℃.

Related to the permeance, the DMC/MeOH selectivity fluctuates slightly at the initial stage of the experiment, and then gradually reaches a steady state (Fig. 10). The SILMs with [ODABCO][Br] and [Omim][NTf2] exhibited higher selectivities than SILMs with [TBA][Br] and [1O3MIm] [Br] at 40℃. In addition, the DMC/MeOH separation performance of SILMs can be tuned by changing the different cation, as observed from Fig. 8, Fig. 9 and Fig. 10 (Table 2). Furthermore, different anions can also lead to different separation performances.

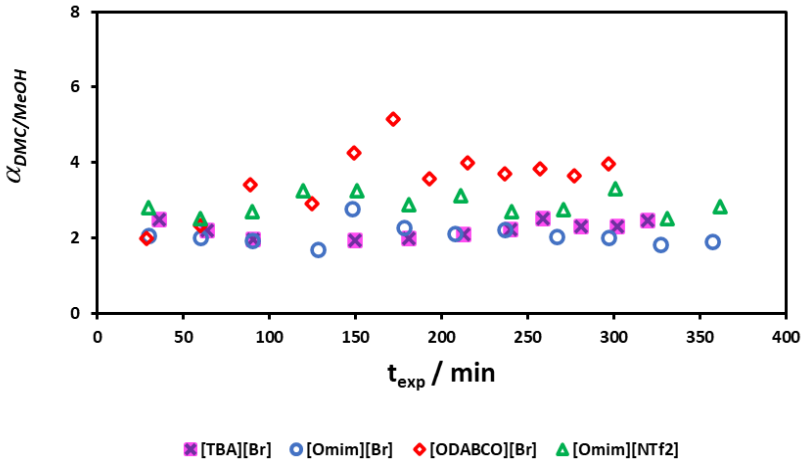

Fig. 10. Selectivity of DMC/MeOH, T= 40 ℃.

Table 2. Permeance and selectivity of SILMs in steady states

	DMC permeance (GPU)	MeOH permeance (GPU)	Selectivity $_{(DMC/MeOH)}$
[TBA][Br]	1059.63 ± 6.03	427.40 ± 16.47	2.48 ± 0.08
[Omim][Br]	1730.93 ± 53.72	859.14 ± 7.09	2.02 ± 0.08
[ODABCO][Br]	1886.77 ± 32.81	487.16 ± 12.78	3.88 ± 0.14
[Omim][NTf2]	1557.67 ± 84.70	520.40 ± 40.90	3.02 ± 0.34

382

383 3.4.2. Effect of operation temperature on permeance and selectivity

384 Experiments at 30, 40 and 50 °C were performed to study the effect of the temperature on DMC and
385 MeOH permeance using SILMs. Fig. 11 shows that MeOH and DMC permeance decreased when the
386 operating temperature increased. All the membranes tested presented a larger DMC permeability
387 compared to MeOH. Specifically, a dramatic decrease of DMC permeance and a slight decrease of
388 MeOH permeance was observed with the increase of temperature, reflecting that DMC permeance
389 across SILMs of [Omim][Br] and [Omim][NTf2] is more sensitive to the temperature. Therefore,
390 MeOH permeance decreased slower than DMC permeance with the increase in temperature, resulting
391 in a decreased selectivity for these two SILMs. For the SILMs with [TBA][Br] and [ODABCO][Br],
392 an increase in selectivity from 40 to 50 °C and from 30 to 40 °C, respectively, was observed. It can be
393 ascribed to the changes in physical states ILs, reflected by DSC. As observed from Fig. 4, the structures
394 of [TBA][Br] and [ODABCO][Br] start to change from around 49 ℃ and 40 ℃, respectively. In
395 summary, the SILMs studied here showed higher selectivities and competitive or even larger
396 permeances at lower temperatures for the separation of DMC from MeOH, especially at 30 °C, in
397 comparison with other membranes (Table 3).

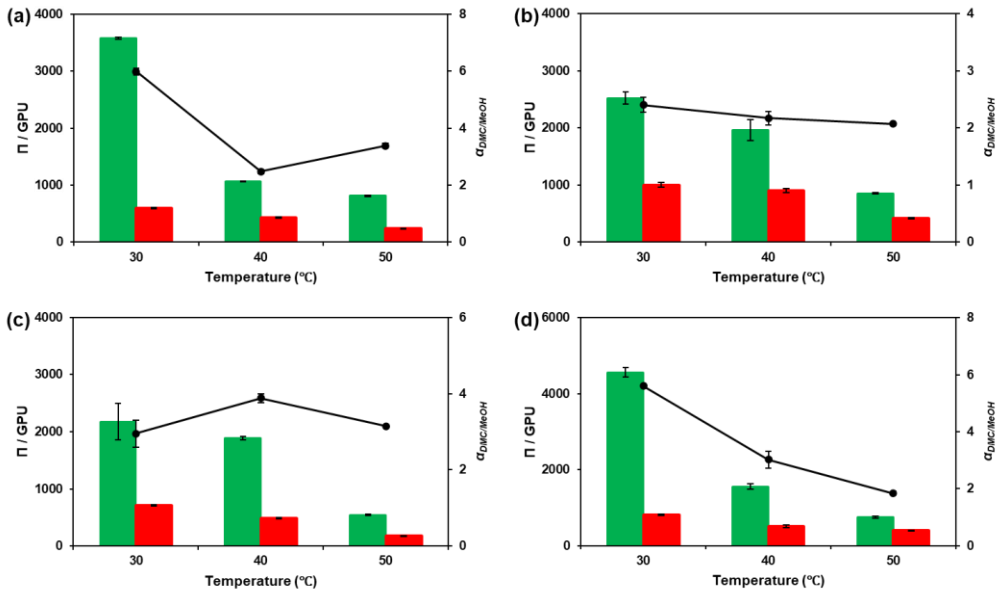

Fig. 11. Effect of operational temperature on permeance and selectivity, (a) SILM of [TBA][Br], (b) SILM of [Omim][Br], (c)SILM of [ODABCO][Br], and (d) SILM of [Omim][NTf2].

Table 3. Comparison with other membranes in the literature

Support	Selective layer	DMC Permeance	Selectivity	Refs.
PVDF	Hydrophobic nano- SiO_2/PDMS	674.41	3.17	[57]
PVDF	PDMS	852.69	3.06	[58]
PVDF	MCM-41 SiO_2-PDMS	469.50	3.18	[59]
PAN	nano SiO_2/RTV	2657.97	3.90	[9]
PAN	[TBA][Br]	3573.84	5.98	**This study**
PAN	[Omim][Br]	2523.04	2.40	**This study**
PAN	[ODABCO][Br]	2175.77	3.88	**This study**
PAN	[Omim][NTf2]	4558.24	5.61	**This study**

To describe the effect of temperature on the permeance, the Arrhenius-type equation (Equation 5) was used[60]. Table 4 summarizes the values of the activation energy obtained from the slope from the graph of the relationship between logarithmic permeance and 1/T. See the Supporting Information (Figs. S11-S14).

Table 4. Activation energy for the investigated membranes.

Membrane	DMC	MeOH
	E_a (J mol^{-1})	E_a (J mol^{-1})
[TBA][Br]	-61.28	-39.05
[Omim][Br]	-44.40	-45.91
[ODABCO][Br]	-56.43	-63.51
[Omim][NTf2]	-76.20	-28.92

A negative activation energy indicates that DMC and MeOH permeances decrease with temperature. The activation energy of component i is the sum of the activation energy of diffusion $E_{D,i}$ and the enthalpy of sorption $\Delta H_{S,i}$ of component i [61]:

$$E_{a,i} = E_{D,i} + \Delta H_{S,i} \quad (5)$$

Since sorption is an exothermic process and diffusion is an endothermic process, the enthalpy of sorption $\Delta H_{S,i}$ is considered negative and the activation energy of diffusion $E_{D,i}$ positive. Therefore, the negative value of $E_{a,i}$ indicates that $\Delta H_{S,i}$ is greater than $E_{D,i}$, with the sorption dominating the transport process of component i across the membrane [61]. As seen in Table 4, for DMC and MeOH, the activation energies were negative, and permeances decrease with the temperature, suggesting that DMC and MeOH permeation through the membrane is controlled by sorption. In addition, the lower the activation energy value, the smaller the effect of the temperature.

3.5 Preliminary pervaporation tests for binary mixtures

In the pervaporation separation of binary mixtures, the coupling effect affected by the feed concentration cannot be neglected [62-64]. As observed in Fig. 12, DMC permeance and selectivity increased with the DMC concentration of the feed. That is, the presence of MeOH affects the permeation of the DMC, and the magnitude of the coupling effect is influenced by the specific feed composition. The smaller MeOH concentration in the feed, the less coupling effect in the pervaporation separation of binary mixture from preliminary results.

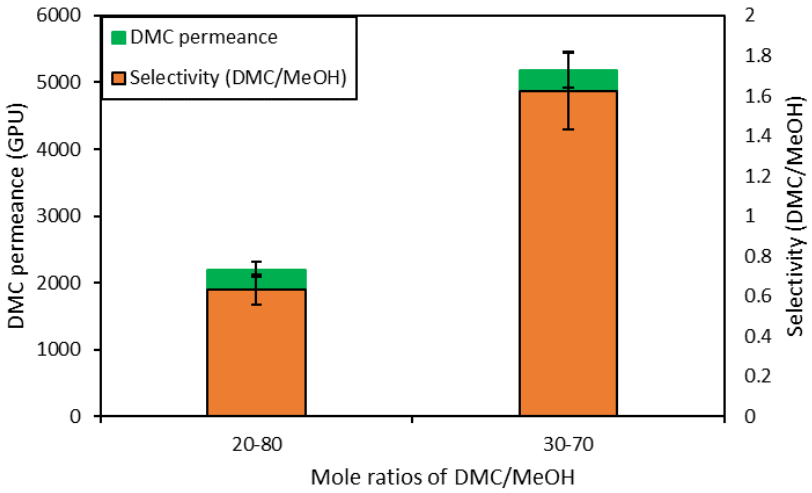

Fig. 12. Pervaporation separation of binary mixtures using SILM of [Omim][Br] at 30℃.

To further analyze the feasibility for application of the task-specific ILs in the separation of DMC from MeOH, a COSMO-RS back-up will be performed in the next section.

3.6. COSMO-RS results

3.6.1. Activity coefficients, σ-profiles and -potentials of the different ILs

Activity coefficients at infinite dilution of a solute can be used to quantify the intermolecular interaction between the solvent and solute, making them particularly useful for solvent selection in extractive operations. They also allow for the approximate calculation of the solute partitioning between a liquid and vapor phase. Furthermore, they provide information on the volatility of a solute [65]. The activity coefficient of a solute *i* can be calculated from its chemical potential in the pure and mixed state [66]:

$$\gamma = \exp\left(\frac{\mu-\mu^0}{RT}\right) \quad (6)$$

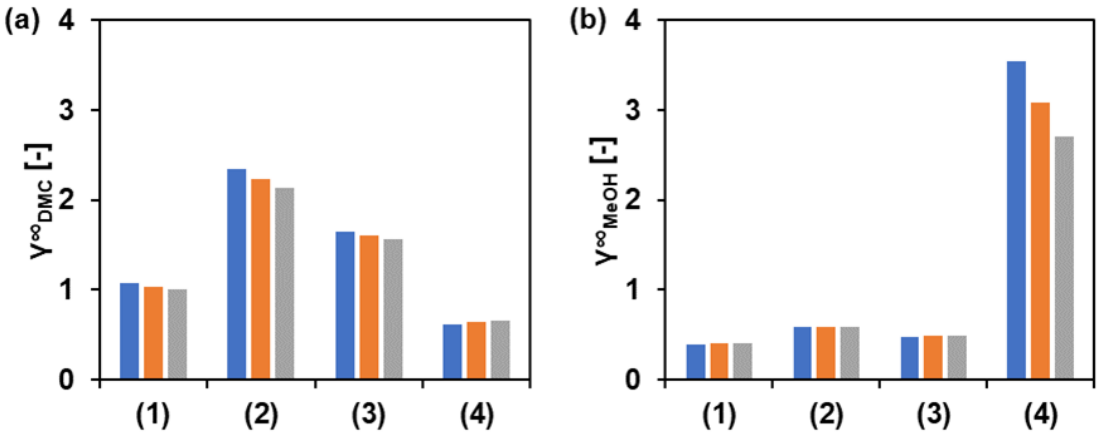

Fig. 13. Activity coefficients of (a) DMC and (b) MeOH in the different ILs at varying temperatures (blue = 30 °C, orange = 40 °C, grey = 50 °C). The ILs are referred to as (1) [TBA][Br], (2) [Omim][Br], (3) [ODABCO][Br], and (4) [Omim][NTf2].

The activity coefficients of MeOH and DMC, calculated as indicated in equation 6 are shown in Fig. 13. The activity coefficient of MeOH is lower than that of DMC (and even lower than unity) for three of the four considered ILs for all temperatures. This indicates that [Omim][Br], [ODABCO][Br] and [TBA][Br] show a higher affinity towards MeOH. The ionic liquid [Omim][NTf2], on the other hand, has a much lower activity coefficient for DMC than for MeOH. This difference in affinity could be explained by the change in the anion structure, as the bis(trifluoromethylsulfonyl)amide anion is much more hydrophobic than the bromide anion. The cation affects the affinity much less than the anion, as shown in Fig. 14, since the [Br]-based ILs have a similar higher affinity to MeOH [65]. Furthermore, it should be noted that for $\gamma^{\infty} < 1$, the activity coefficient will increase at higher temperatures, whilst the opposite holds for $\gamma^{\infty} > 1$. This was also observed by Matheswaran et al. [67] for IL-thiophene systems.

The higher affinity for MeOH in certain cases can be linked to the σ-profiles and -potentials of the solvents and the different ILs. The anion and cation of the ILs cause positive and negative screening

charge densities, respectively. Therefore, they will show up in the acceptor and donor region of the σ-profile, respectively. It should be noted that the non-polarity of ILs is affected by both cation and anion structures. These profiles can be split into three regions: (1) a H-bond donor region ($\sigma < -0.0084$ e Å^{-2}), (2) a H-bond acceptor region ($\sigma > +0.0084$ e Å^{-2}), and (3) a non-polar region (-0.0084 e Å $- 2 < \sigma < +0.0084$ e Å^{-2}). Referring to the σ surface of molecules shown in Fig. 14, the red region indicates the positive of hydrogen bond acceptors. On the other hand, the blue region represents the hydrogen bond donors. The green region shows the non-polar part of the compound.

From Fig. 14 (a), it is clear that the σ-profile of DMC presents the largest peaks within the non-polar region, and smaller peaks in the H-bond acceptor region, due to the ketone group. MeOH, on the other hand, shows the ability to engage in both H-bond donor and acceptor interactions, due to its peaks in both regions, as can be seen in Fig. 14 (b). As observed in Fig. 14 (c)-(f), [Omim][NTf2] and [TBA][Br] are more non-polar in nature than the other ILs, since the greater part of their peaks lies within the non-polar region. The non-polarity of [Omim][NTf2] is primarily caused by an inefficient charge delocalization caused by the [NTf2]-anion, while the non-polarity of [TBA][Br] is dominated by partially electropositive sides of [TBA]-cation [68, 69]. However, the [Br]-anion shows stronger peak in the hydrogen bonding acceptor zones compared than [NTf2]-anion [68, 70]. Thus, [NTf2]-based IL requires more interaction energies to be broken for the dissolution of a MeOH molecule than [Br]-based IL for ILs containing the same cation. Similar conclusions can be drawn from the σ-potentials, as depicted in Figs. S15-S16.

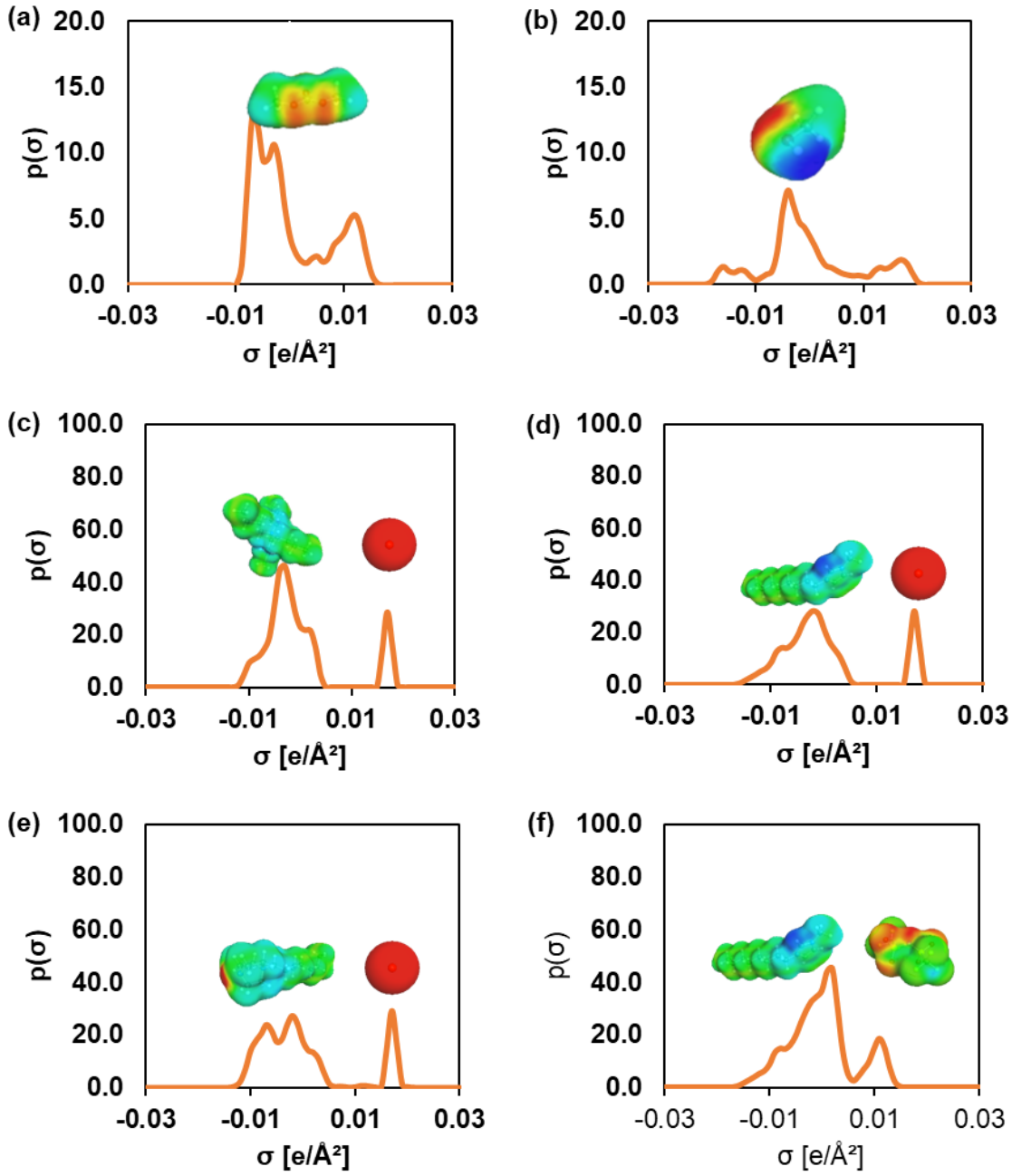

Fig. 14. σ-profiles and -surfaces of the considered solvents (a) DMC and (b) MeOH, and the considered ILs (c) [TBA][Br], (d) [Omim][Br], (e) [ODABCO][Br], and (f) [Omim][NTf2].

3.6.2 Predicted DMC/MeOH-selectivity of the different ILs

Next to activity coefficients at infinite dilution, the selectivity S_{ij}^{∞} for a specific separation case can be calculated as follows:

$$S_{ij}^{\infty} = \frac{\gamma_j^{\infty}}{\gamma_i^{\infty}} \quad (7)$$

Based on this value, it can be estimated whether an IL can act as an effective extractant (if $S_{ij}^{\infty} \gg 1$) or not (if $S_{ij}^{\infty} \sim 1$) [66]. As mentioned above, the experimental selectivities are calculated based on the permeance rates of both solvents.

The simulated and experimental DMC/MeOH-selectivities are presented in Fig. 15 (a) and (b), respectively. It should be noted that an exact comparison is not applicable, since COSMO-RS only takes the solubility and solute-solvent affinity into account. The actual experimental selectivity based on the permeance is also dependent on the diffusivity of the solute in the solvent [71].

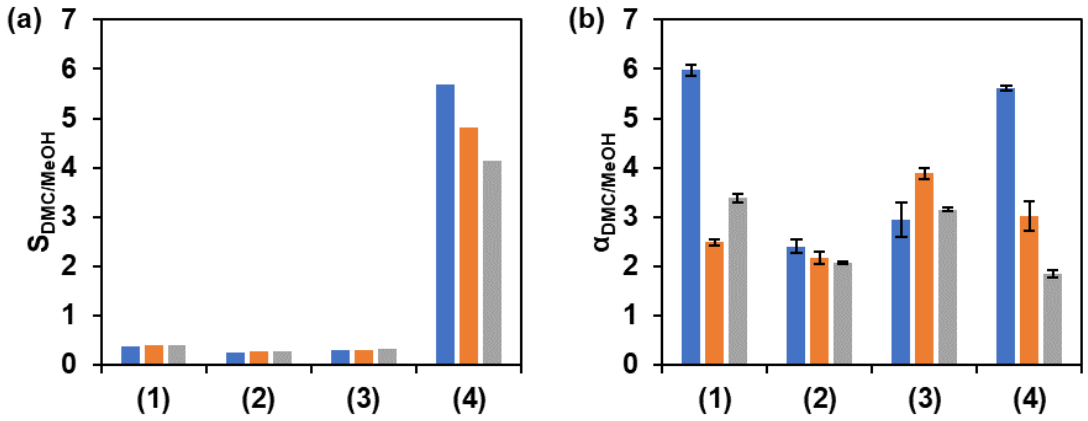

Fig. 15. Simulated (a) and experimental (b) DMC/MeOH-selectivities in the different ionic liquids at varying temperatures (blue = 30 °C, orange = 40 °C, grey = 50 °C). The ILs are referred to as (1) [TBA][Br], (2) [Omim][Br], (3) [ODABCO][Br], and (4) [Omim][NTf2].

The result from Fig. 15 (a), suggest that [Omim][NTf2] presents the highest selectivity, which decreases with increasing temperature. This is due to a higher affinity for MeOH at higher temperatures, as is indicated by the lower activity coefficient of MeOH in Fig. 13 (b). For the [Br]-based ILs, a slight increase in the selectivity is visible, due to a decrease in the activity coefficient for DMC at higher temperatures. Moreover, the COSMO-RS simulations would suggest that, taking into account only the solubilities, the [Br]-based ILs would not be selective towards DMC, since their selectivity is less than unity. This is not observed in the experimental selectivities, which indicate that all the ILs show a selectivity towards DMC. However, it can be also seen that [Omim][NTf2] shows the hight selectivity at a temperature of 30 °C. This was also predicted by COSMO-RS, based on the activity coefficients. At higher temperatures, the selectivity decreases for SILMs with [Omim][Br] and [Omim][NTf2], except for SILMs with [TBA][Br] and [ODABCO][Br], which show an even higher selectivity than [Omim][NTf2] at 50 °C.

The discrepancies between the experimental and simulated data may be caused by multiple factors. First, COSMO does not take diffusivity and diffusivity into account and solely looks at solubility, as stated before. The diffusivity could be calculated using molecular dynamics simulations, as presented

in the paper by Arenas [71] for the extraction of naphthenic acid. Besides that, [TBA][Br] and [ODABCO][Br] are in the solid state over the whole pervaporation temperature range, but the COSMO-RS method can only allow calculation of the (pseudo) chemical potential of compounds in liquid and gas phases[72]. Moreover, both ILs underwent certain structural transitions according to above-mentioned thermal properties. However, this lies beyond the scope of this screening since the main goal is to understand the membrane performance at molecular level. In section 3.4.2 the results showed that solubility was the main mechanism leading the mass transfer. Thus, it makes sense that the COSMO-RS results qualitatively describe high affinity of the ionic liquid [Omim][NTf2].

Nevertheless, those preliminary predictions could be taken as a first screening, but experimental validation is always advisable. As stated by Paduszynski et al. [66], COSMO-RS has difficulties in providing quantitatively accurate results and is known for underpredicting the actual values of activity coefficients. This is especially the case for molecules with a high degree of conformational flexibility, such as long chain *n*-alkanes. Still, COSMO-RS seems to provide qualitative trends and provides a useful tool in initial solvent screening.

4. Conclusions

Three ILs namely, 1-octyl-3-methylimidazolium bromide ([Omim][Br]), 1-Octyl-1,4-diazabicyclo[2.2.2]octanium bromide ([ODABCO][Br]) and 1-Octyl-3-methylimidazolium bis(trifluoromethanesulfonyl)imide ([Omim][NTf2]) were synthesized, and their structure as well as purity were confirmed by NMR. Thermal properties of the as-synthesized ILs and one commercial IL tetrabutylammonium bromide ([TBA][Br]) were investigated. The four ILs [Omim][Br], [ODABCO][Br], [Omim][NTf2] and [TBA][Br] were immobilized on porous PAN supports to prepare SILMs. The SILMs were characterized by SEM-EDX, tensile stress tests and stability tests in pure solvents. These studies showed that the ILs were successfully immobilized on the membrane and that SILMs were stable when it was exposed to DMC and MeOH. Incorporation of IL into the PAN pores reduced both the elasticity and ductility of the membranes compared to PAN. Pure liquid (DMC or MeOH) pervaporation experiments were carried out in a pervaporation set-up at different temperatures. The temperature was observed to play a very important role in the permeance and selectivity. DMC and MeOH permeance decreased when the operating temperature increased, indicating a sorption dominated transport. All membranes preferentially permeated DMC having a selectivity larger than 1. All the studied SILMs presented a decrease in permeance and selectivity as a whole with temperature except the SILMs with [ODABCO][Br]. DMC permeance computed for the SILMs was far greater than MeOH permeance, especially at lower temperature. Furthermore, these SILMs presented higher DMC permeances and selectivity of DMC/MeOH at low temperatures, especially at 30 °C. In addition, the COSMO-RS model was used as a theoretical tool to provide molecular level insights into the separation

of DMC from MeOH using SILMs. In short, the results of this study are encouraging for the separation of DMC from MeOH using SILMs, which also lay a groundwork for converting CO_2 into value-added products by the convergence of catalytical ILs with membrane separation processes.

Acknowledgments

The authors acknowledge the funding from the China Scholarship Council (CSC, No.201906050060) and the Flemish Strategic Basic Research Program of the Catalisti cluster and Flanders Innovation & Entrepreneurship in the framework of the EASiCHEM project (contracts HBC.2018.0484 and K200522N). This work was partly developed within the scope of the project CICECO-Aveiro Institute of Materials, UIDB/50011/2020, UIDP/50011/2020 & LA/P/0006/2020, financed by national funds through the FCT/MEC (PIDDAC). Thank you to Professor Pedro Carvalho for discussion and constructive suggestions and to Professor Damien Debecker for his generous help with material characterizations.

References

1. Xu, X., et al., *High-performance ZIF-8/biopolymer chitosan mixed-matrix pervaporation membrane for methanol/dimethyl carbonate separation.* Separation and Purification Technology, 2022. **293**: p. 121085.
2. Esan, A.O., A.D. Adeyemi, and S. Ganesan, *A review on the recent application of dimethyl carbonate in sustainable biodiesel production.* Journal of Cleaner Production, 2020. **257**: p. 120561.
3. Keller, N., G. Rebmann, and V. Keller, *Catalysts, mechanisms and industrial processes for the dimethylcarbonate synthesis.* Journal of Molecular Catalysis A: Chemical, 2010. **317**(1-2): p. 1-18.
4. Shaikh, A.-A.G. and S. Sivaram, *Organic carbonates.* Chemical reviews, 1996. **96**(3): p. 951-976.
5. Wang, J., et al., *Superconcentrated electrolytes for a high-voltage lithium-ion battery.* Nature communications, 2016. **7**(1): p. 1-9.
6. Kawamura, T., et al., *Thermal stability of alkyl carbonate mixed-solvent electrolytes for lithium ion cells.* Journal of Power Sources, 2002. **104**(2): p. 260-264.
7. Alfreider, A., M. Schirmer, and C. Vogt, *Diversity and expression of different forms of RubisCO genes in polluted groundwater under different redox conditions.* FEMS microbiology ecology, 2012. **79**(3): p. 649-660.
8. Pacheco, M.A. and C.L. Marshall, *Review of dimethyl carbonate (DMC) manufacture and its characteristics as a fuel additive.* Energy & Fuels, 1997. **11**(1): p. 2-29.
9. Liu, Z., et al., *Separation of dimethyl carbonate/methanol azeotropic mixture by pervaporation with dealcoholized room temperature-vulcanized silicone rubber/nanosilica hybrid active layer.* Separation and Purification Technology, 2020. **248**: p. 116926.
10. Lin, H., et al., *Kinetics studies for the synthesis of dimethyl carbonate from urea and methanol.* Chemical Engineering Journal, 2004. **103**(1-3): p. 21-27.
11. Cai, Q., et al., *Studies on synthesis of dimethyl carbonate from methanol and carbon dioxide.* Catalysis Communications, 2009. **10**(5): p. 605-609.
12. Zhao, T., et al., *Direct synthesis of dimethyl carbonate from carbon dioxide and methanol at room temperature using imidazolium hydrogen carbonate ionic liquid as a recyclable catalyst and dehydrant.* ChemSusChem, 2017. **10**(9): p. 2046-2052.
13. Eta, V., et al., *Synthesis of dimethyl carbonate from methanol and carbon dioxide: circumventing thermodynamic limitations.* Industrial & engineering chemistry research, 2010. **49**(20): p. 9609-9617.
14. Jessop, P.G., T. Ikariya, and R. Noyori, *Homogeneous hydrogenation of carbon dioxide.* Chemical Reviews, 1995. **95**(2): p. 259-272.
15. Hu, J., et al., *Zinc (II)-catalyzed reactions of carbon dioxide and propargylic alcohols to carbonates at room temperature.* Green Chemistry, 2016. **18**(2): p. 382-385.
16. Honda, M., et al., *Ceria‐catalyzed conversion of carbon dioxide into dimethyl carbonate with 2‐cyanopyridine.* ChemSusChem, 2013. **6**(8): p. 1341-1344.
17. Brennecke, J.F. and E.J. Maginn, *Ionic liquids: innovative fluids for chemical processing.* American Institute of Chemical Engineers. AIChE Journal, 2001. **47**(11): p. 2384.
18. Rynkowska, E., K. Fatyeyeva, and W. Kujawski, *Application of polymer-based membranes containing ionic liquids in membrane separation processes: a critical review.* Reviews in Chemical Engineering, 2018. **34**(3): p. 341-363.
19. Wilkes, J.S., *A short history of ionic liquids—from molten salts to neoteric solvents.* Green Chemistry, 2002. **4**(2): p. 73-80.
20. Pârvulescu, V.I. and C. Hardacre, *Catalysis in ionic liquids.* Chemical Reviews, 2007. **107**(6): p. 2615-2665.

21. Li, J., et al., *Quaternary ammonium ionic liquids as bi-functional catalysts for one-step synthesis of dimethyl carbonate from ethylene oxide, carbon dioxide and methanol.* Catalysis letters, 2011. **141**(2): p. 339-346.
22. Tsuru, T., et al., *Pervaporation of methanol/dimethyl carbonate using SiO2 membranes with nano‐tuned pore sizes and surface chemistry.* AIChE journal, 2011. **57**(8): p. 2079-2089.
23. Zhu, T., et al., *Pervaporation separation of dimethyl carbonate/methanol azeotrope through cross-linked PVA–poly (vinyl pyrrolidone)/PAN composite membranes.* Desalination and Water Treatment, 2013. **51**(28-30): p. 5485-5493.
24. He, Y., et al., *Control of extractive distillation processes with intermediate impurities removed as a side withdrawal from the extractive distillation column.* Journal of Chemical Technology & Biotechnology, 2020. **95**(5): p. 1487-1502.
25. Luis, P., *Fundamental Modeling of Membrane Systems: Membrane and Process Performance*. 2018: Elsevier.
26. Xu, X., et al., *MOF-based membranes for pervaporation.* Separation and Purification Technology, 2021. **278**: p. 119233.
27. Plechkova, N.V. and K.R. Seddon, *Applications of ionic liquids in the chemical industry.* Chemical Society Reviews, 2008. **37**(1): p. 123-150.
28. Li, W., et al., *Supported ionic liquid membranes for the separation of methanol/dimethyl carbonate mixtures by pervaporation.* Journal of Membrane Science, 2020. **598**: p. 117790.
29. Izák, P., et al., *Catalytic Ionic‐Liquid Membranes: The Convergence of Ionic‐Liquid Catalysis and Ionic‐Liquid Membrane Separation Technologies.* ChemPlusChem, 2018. **83**(1): p. 7-18.
30. Sasikumar, B., G. Arthanareeswaran, and A. Ismail, *Recent progress in ionic liquid membranes for gas separation.* Journal of Molecular Liquids, 2018. **266**: p. 330-341.
31. Karkhanechi, H., S. Salmani, and M. Asghari, *A review on gas separation applications of supported ionic liquid membranes.* ChemBioEng Reviews, 2015. **2**(4): p. 290-302.
32. Liu, Z., et al., *CO2 separation by supported ionic liquid membranes and prediction of separation performance.* International Journal of Greenhouse Gas Control, 2016. **53**: p. 79-84.
33. Cserjési, P., N. Nemestóthy, and K. Bélafi-Bakó, *Gas separation properties of supported liquid membranes prepared with unconventional ionic liquids.* Journal of Membrane Science, 2010. **349**(1-2): p. 6-11.
34. Althuluth, M., et al., *Natural gas purification using supported ionic liquid membrane.* Journal of Membrane Science, 2015. **484**: p. 80-86.
35. Zhang, X., et al., *Selective separation of H2S and CO2 from CH4 by supported ionic liquid membranes.* Journal of Membrane Science, 2017. **543**: p. 282-287.
36. Jiang, Y.-Y., et al., *SO2 gas separation using supported ionic liquid membranes.* The Journal of Physical Chemistry B, 2007. **111**(19): p. 5058-5061.
37. Ilyas, A., et al., *Supported protic ionic liquid membrane based on 3-(trimethoxysilyl) propan-1-aminium acetate for the highly selective separation of CO2.* Journal of Membrane Science, 2017. **543**: p. 301-309.
38. Zhang, P., et al., *Natural deep eutectic solvent-based gels with multi-site interaction mechanism for selective membrane separation of SO2 from N2 and CO2.* Chemical Engineering Journal, 2022. **438**: p. 135626.
39. Peng, L., et al., *Facilitated transport separation of CO2 and H2S by supported liquid membrane based on task-specific protic ionic liquids.* Green Chemical Engineering, 2022.
40. Tu, Z., et al., *Selective and simultaneous membrane separation of CO and H2 from N2 by protic chlorocuprate ionic liquids.* Renewable Energy, 2022. **196**: p. 912-920.
41. Zhang, X., et al., *Supported ionic liquid membranes with dual-site interaction mechanism for efficient separation of CO2.* ACS Sustainable Chemistry & Engineering, 2019. **7**(12): p. 10792-10799.

42. Pei, Y., et al., *Liquid− liquid equilibria of aqueous biphasic systems containing selected imidazolium ionic liquids and salts.* Journal of Chemical & Engineering Data, 2007. **52**(5): p. 2026-2031.
43. Weber, S., et al., *Selective Hydrogenation of Aldehydes Using a Well‐Defined Fe (II) PNP Pincer Complex in Biphasic Medium.* ChemCatChem, 2018. **10**(19): p. 4386-4394.
44. Lee, B.-C. and S.L. Outcalt, *Solubilities of gases in the ionic liquid 1-n-butyl-3-methylimidazolium bis (trifluoromethylsulfonyl) imide.* Journal of Chemical & Engineering Data, 2006. **51**(3): p. 892-897.
45. Li, W., et al., *Sorption and pervaporation study of methanol/dimethyl carbonate mixture with poly (etheretherketone)(PEEK-WC) membrane.* Journal of Membrane Science, 2018. **567**: p. 303-310.
46. Khan, H.W., et al., *Screening of ionic liquids for the extraction of biologically active compounds using emulsion liquid membrane: COSMO-RS prediction and experiments.* Journal of Molecular Liquids, 2020. **309**: p. 113122.
47. Zhang, Z., et al., *COSMO‐RS based ionic liquid screening for the separation of acetonitrile and ethanol azeotropic mixture.* Journal of Chemical Technology & Biotechnology, 2020. **95**(4): p. 1191-1202.
48. Wojeicchowski, J.P., et al., *Extraction of phenolic compounds from rosemary using choline chloride–based deep eutectic solvents.* Separation and Purification Technology, 2021. **258**: p. 117975.
49. Fetouhi, B., et al., *Synthesis, molecular structure, and properties of DABCO bromide based ionic liquid combining spectroscopic studies with DFT calculations.* Journal of Molecular Structure, 2021. **1233**: p. 130102.
50. Perez, S.J.L. and S. Arco, *Synthesis and Characterization of 1-Octyl-3-Methylimidazolium Bromide [OMIM]Br Ionic Liquid As A Potential Antifungal Agent*. 2013.
51. Rout, A., et al., *Room temperature ionic liquid diluent for the mutual separation of europium (III) from americium (III).* Separation and purification technology, 2011. **81**(2): p. 109-115.
52. Lauw, Y., et al., *Structural studies on the basic ionic liquid 1-ethyl-1, 4-diazabicyclo [2.2. 2] octanium bis (trifluoromethylsulfonyl) imide and its bromide precursor.* Crystal growth & design, 2012. **12**(6): p. 2803-2813.
53. Cichowska-Kopczyńska, I., et al., *Influence of ionic liquid structure on supported ionic liquid membranes effectiveness in carbon dioxide/methane separation.* Journal of Chemistry, 2013. **2013**.
54. Narducci, R., et al., *Mechanical properties of anion exchange membranes by combination of tensile stress–strain tests and dynamic mechanical analysis.* Journal of Polymer Science Part B: Polymer Physics, 2016. **54**(12): p. 1180-1187.
55. Hernández-Fernández, F.J., et al., *A novel application of supported liquid membranes based on ionic liquids to the selective simultaneous separation of the substrates and products of a transesterification reaction.* Journal of Membrane Science, 2007. **293**(1-2): p. 73-80.
56. Munshi, M.K., et al., *Role of cation–anion cooperation in the selective synthesis of glycidol from glycerol using DABCO–DMC ionic liquid as catalyst.* Rsc Advances, 2014. **4**(61): p. 32127-32133.
57. Wang, L., et al., *Hydrophobic nano-silica/polydimethylsiloxane membrane for dimethylcarbonate–methanol separation via pervaporation.* Chemical engineering journal, 2011. **171**(3): p. 1035-1044.
58. Zhou, H., et al., *PDMS/PVDF composite pervaporation membrane for the separation of dimethyl carbonate from a methanol solution.* Journal of membrane science, 2014. **471**: p. 47-55.
59. Wang, L., et al., *Modified MCM‐41 silica spheres filled polydimethylsiloxane membrane for dimethylcarbonate/methanol separation via pervaporation.* Journal of applied polymer science, 2013. **127**(6): p. 4662-4671.

60. Li, W., et al., *Application of pervaporation in the bio-production of glycerol carbonate.* Chemical Engineering and Processing-Process Intensification, 2018. **132**: p. 127-136.
61. Luis, P., J. Degrève, and B. Van der Bruggen, *Separation of methanol–n-butyl acetate mixtures by pervaporation: potential of 10 commercial membranes.* Journal of membrane science, 2013. **429**: p. 1-12.
62. Niemistö, J., W. Kujawski, and R.L. Keiski, *Pervaporation performance of composite poly (dimethyl siloxane) membrane for butanol recovery from model solutions.* Journal of Membrane Science, 2013. **434**: p. 55-64.
63. Won, W., X. Feng, and D. Lawless, *Separation of dimethyl carbonate/methanol/water mixtures by pervaporation using crosslinked chitosan membranes.* Separation and purification technology, 2003. **31**(2): p. 129-140.
64. Li, W. and P. Luis, *Understanding coupling effects in pervaporation of multi-component mixtures.* Separation and Purification Technology, 2018. **197**: p. 95-106.
65. Banerjee, T. and A. Khanna, *Infinite dilution activity coefficients for trihexyltetradecyl phosphonium ionic liquids: measurements and COSMO-RS prediction.* Journal of Chemical & Engineering Data, 2006. **51**(6): p. 2170-2177.
66. Paduszyński, K., *An overview of the performance of the COSMO-RS approach in predicting the activity coefficients of molecular solutes in ionic liquids and derived properties at infinite dilution.* Physical Chemistry Chemical Physics, 2017. **19**(19): p. 11835-11850.
67. Matheswaran, P., et al., *Overview of activity coefficient of thiophene at infinite dilution in ionic liquids and their modeling using COSMO-RS.* Industrial & Engineering Chemistry Research, 2016. **55**(3): p. 788-797.
68. Yu, G., et al., *Structural effect on the vapor-liquid equilibrium of toluene-ionic liquid systems.* Chemical Engineering Science, 2019. **198**: p. 1-15.
69. Qin, Z., et al., *Selection of deep eutectic solvents for extractive deterpenation of lemon essential oil.* Journal of Molecular Liquids, 2022: p. 118524.
70. Klamt, A., *COSMO-RS for aqueous solvation and interfaces.* Fluid Phase Equilibria, 2016. **407**: p. 152-158.
71. Arenas, P., I. Suárez, and B. Coto, *Combination of molecular dynamics simulation, COSMO-RS, and experimental study to understand extraction of naphthenic acid.* Separation and Purification Technology, 2022. **280**: p. 119810.
72. Klamt, A., et al., *Refinement and parametrization of COSMO-RS.* The Journal of Physical Chemistry A, 1998. **102**(26): p. 5074-5085.